CORE
Metadata, citation and similar papers at core.ac.uk
Provided by Bradford Scholars

Journal of Hydraulic Research Vol. 44, No. 3 (2006), pp. 338–349
© 2006 International Association of Hydraulic Engineering and Research

Simulation of breaking wave by SPH method coupled with k–ϵ model

Simulation des vagues déferlantes par la méthode SPH couplée à un modèle k–ϵ

SONGDONG SHAO, Associate Professor, *Research Institute of Water Resources and Hydro-electric Engineering, North China Electric Power University, Zhuxinzhuang, Deshengmenwai, Beijing 102206, China. Tel.: 0086-10-62919133; e-mail: songdongshao@hotmail.com.*

ABSTRACT
The paper employs a Reynolds-averaged Navier–Stokes (RANS) approach to investigate the time-dependent wave breaking processes. The numerical model is the smoothed particle hydrodynamic (SPH) method. It is a mesh-free particle approach which is capable of tracking the free surfaces of large deformation in an easy and accurate way. The widely used two-equation k–ε model is chosen as the turbulence model to couple with the incompressible SPH scheme. The numerical model is employed to reproduce cnoidal wave breaking on a slope under two different breaking conditions—spilling and plunging. The computed free surface displacements, turbulence intensities and undertow profiles are in good agreement with the experimental data and other numerical results. According to the computations, the breaking wave characteristics are presented and discussed. It is shown that the SPH method provides a useful tool to investigate the surf zone dynamics.

RÉSUMÉ
L'article utilise une approche RANS pour étudier les processus de déferlement des vagues en fonction du temps. Le modèle numérique est la méthode des particules hydrodynamiques lissées (SPH). C'est une approche particulaire sans maillage qui est capable de dépister et de suivre les surfaces libres soumises à de grandes déformations, facilement et de manière précise. Le modèle à deux équations largement répandu k–ϵ est choisi comme modèle de turbulence pour être couplé avec le schéma incompressible SPH. Le modèle numérique est utilisé pour reproduire le déferlement sur une pente d'une onde cnoïdale sous deux conditions différentes de déferlement—déversant et plongeant. Les déplacements calculés de la surface libre, les intensités de turbulence et les profils du contre-courant de fond sont en bon accord avec les données expérimentales et d'autres résultats numériques. Selon les calculs, les caractéristiques des vagues déferlantes sont présentées et discutées. On montre que la méthode SPH fournit un outil utile pour étudier la dynamique des zones de ressac.

Keywords: SPH, k–ϵ model, breaking wave, incompressible.

1 Introduction

Coastal waves break in a region called the surf zone, which is characterized by the irreversible transformation of organized wave motions into motions of different types and scales including the turbulence, vortices, low frequency waves and currents. The swash zone is identified as the part of the beach between the minimum and maximum water levels during the wave running up and down. The knowledge of wave breaking is very essential to nearly all of the coastal processes, such as the coastal current, sediment and pollutant transport and wave forces on coastal structures. Excellent reviews on the research progress of surf and swash zone dynamics have been made by Ting and Kirby (1994, 1995, 1996), Lin and Liu (1998a, b), Bradford (2000) and Longo *et al.* (2002).

The wave breaking process must be clarified in order to solve many coastal problems. However, the study of breaking waves is a difficult task for a number of reasons. For example, the velocity field during breaking is extremely chaotic and varies rapidly in time. The difficulties of measuring velocity due to the existence of air bubbles entrained by the plunging jet have hindered many experimental studies on the wave breaking. Field studies also suffer from the same difficulties as the experiments and, in addition, are hindered by limited site access and environmental variability (Bradford, 2000). For these practical reasons, the numerical studies of breaking waves have become increasingly popular in that the numerical simulations can provide flow details without scaling and observational difficulties. As far as the current knowledge is concerned, numerical models based on the full Reynolds-averaged Navier–Stokes (RANS) equations might be the most powerful tool to deal with the time-dependent flows including the breaking waves. Combined with the free surface tracking techniques such as the MAC (Harlow and Welch, 1965) and VOF (Hirt and Nichols, 1981) methods, the RANS models have been extensively employed and validated in the costal hydrodynamics through the implementation of the finite difference, finite volume or finite element schemes.

Revision received March 15, 2005/Open for discussion until May 31, 2007.

In contrast to the commonly used Eulerian grid method, a particle model has the great advantage in that the particles move in Lagrangian coordinates and the advection in the N–S equations is directly calculated by particle motion without the numerical diffusion. The numerical diffusion becomes a severe problem when the deformation of free surface is large. The particle model employed in this paper is developed based on the smoothed particle hydrodynamics (SPH) method (Monaghan, 1992). SPH is a mesh-free particle approach which was originally from the astrophysics and later extended to the fluid flows. In the original applications of SPH to the fluid flow, the fluid was assumed to be weakly compressible and an equation of state was introduced to calculate the pressure. Besides, the solid boundary treatment was implemented through a force function. Recently an incompressible SPH model has been put forward by Shao and Lo (2003), in which the pressure was calculated through a pressure Poisson equation derived from combinations of the mass and momentum equations. The boundary treatment and solution process are also very similar to those employed in a grid method. Thus the incompressible SPH model serves as a good link between the particle and grid modeling techniques. The incompressible SPH model has proved to be a robust way for free surface tracking through the applications of a regular wave interacting with the breakwater (Gotoh *et al.*, 2004) and a solitary wave breaking on the beach (Shao and Gotoh, 2005). The breaking waves were also studied by Koshizuka *et al.* (1998) using the moving particle semi-implicit (MPS) method (Koshizuka *et al.*, 1995), which clearly showed the differences between a spilling and plunging breaker for a cnoidal wave.

Turbulence modeling is another key issue to be addressed in the analyses of breaking waves. For the non-breaking waves, the potential flow theory can be used with enough accuracy. While for the breaking waves, the flow becomes highly rotational and complicated, thus necessitating the implementation of more sophisticated descriptions of wave dynamics. At the current stage, direct numerical simulation (DNS) is impossible for the high Reynolds number flows in large computational domains. Large eddy simulation (LES) has been put forward to balance the computational accuracy and efficiency (Rogallo and Moin, 1984). However, LES still needs a very fine grid and this requirement cannot easily be achieved in practice. Although the LES modeling was tried by Gotoh *et al.* (2004) for a regular wave interacting with the breakwater, the spatial resolution was not fine enough to capture the detailed flow properties such as small eddies, so the essence of real LES could not be fully explored. On the other hand, the RANS equations coupled with different turbulence closure models have enjoyed great successes in a wide variety of practical fields. Turbulence stresses in the RANS equations can be closed using any of the existing turbulence models. No single turbulence model is accepted universally for solving all classes of problem but each model has certain advantages over the other depending on the type and nature of the flow field to be simulated and the desired accuracy of results. Among the existing turbulence closure schemes, the two-equation k–ε model is the most popular one which has undergone numerous tests. For example, Lin and Liu (1998a, b) successfully employed a nonlinear k–ε model to investigate two different breaking waves in the surf zone. The same problem was later addressed by Bradford (2000) and meanwhile a detailed comparison was also made for the three different turbulence models.

Until now it seems that no specific turbulence model has ever been designed for the SPH method. Monaghan (2002) put forward the conception of compressible turbulence in an SPH method. The proposed SPH alpha model is an extension of the original XSPH algorithm, which aimed to reduce the particle disorder at short length scales and retain the constants of motion. Besides, Shao and Gotoh (2005) used a 2D sub-particle scale turbulence model based on the eddy viscosity assumption to simulate a wave breaking on the beach. A similar turbulence modeling technique was also used by Violeau *et al.* (2001) for a Poiseuille turbulence flow. Here a more widely used two-equation k–ε model is to be incorporated into the basic SPH numerical scheme.

The paper is organized in the following ways. First, an incompressible SPH method is developed using the RANS equations and a two-equation k–ε model is formulated using the particle approach. Then the numerical model is employed to reproduce the wave breaking experiment of Ting and Kirby (1994). Flow characteristics of the spilling and plunging breakers are discussed based on the simulation results. Finally, we fully employ the advantages of numerical modeling to disclose fundamental differences between the two types of breakers by investigating the temporal and spatial evolutions of turbulence quantities.

2 Navier–Stokes equations and turbulence model

2.1 Navier–Stokes equations

Employing an SPH particle approach, the RANS equations are presented in the Lagrangian form as

$$\frac{1}{\rho}\frac{\mathrm{D}\rho}{\mathrm{D}t} + \nabla \cdot \mathbf{u} = 0 \tag{1}$$

$$\frac{\mathrm{D}\mathbf{u}}{\mathrm{D}t} = -\frac{1}{\rho}\nabla P + \mathbf{g} + \nu_0 \nabla^2 \mathbf{u} + \frac{1}{\rho}\nabla \cdot \overrightarrow{\tau} \tag{2}$$

where ρ = density; t = time; $\mathbf{u}$ = velocity; P = pressure; $\mathbf{g}$ = gravitational acceleration; ν_0 = kinematic viscosity of laminar flow and $\overrightarrow{\tau}$ = Reynolds stress. The mass conservation equation (1) is written in the form of a compressible flow using a full derivative. The purpose is to impose the incompressibility by setting $\mathrm{D}\rho/\mathrm{D}t = 0$ at fluid particles during the semi-implicit SPH computations.

2.2 Two-equation k–ε turbulence model

The k–ε model has enjoyed great popularity in the numerical hydrodynamics. It is an important turbulence closure model on a level lower than the Reynolds stress closure model. In the k–ε model, instead of seeking the direct closure of the Reynolds stress transport equations, an eddy viscosity assumption is made to relate the Reynolds stress $\overrightarrow{\tau}$ (with each element denoted by τ_{ij})

in Eq. (2) to the turbulence kinetic energy k and the strain rate of mean flow as

$$\frac{\tau_{ij}}{\rho} = 2\nu_{\mathrm{T}} S_{ij} - \frac{2}{3}k\delta_{ij} \tag{3}$$

where $S_{ij} = \frac{1}{2}(\partial u_i/\partial x_j + \partial u_j/\partial x_i)$ is the element of mean strain rate; ν_{T} = turbulence eddy viscosity and δ_{ij} = Kronecker delta.

By assuming the local balance of the turbulence production and dissipation and using a dimensional analysis, the relationship between the turbulence eddy viscosity ν_{T}, turbulence energy k and turbulence dissipation rate ε is established as follows

$$\nu_{\mathrm{T}} = c_{\mathrm{d}}\frac{k^2}{\varepsilon} \tag{4}$$

where c_{d} = empirical constant.

The k and ε transport equations are derived from the N–S equations and represented in the following form for the SPH particle approach as

$$\frac{\mathrm{D}k}{\mathrm{D}t} = \nabla\cdot\left(\frac{\nu_{\mathrm{T}}}{\sigma_k}\nabla k\right) + P_k - \varepsilon \tag{5}$$

$$\frac{\mathrm{D}\varepsilon}{\mathrm{D}t} = \nabla\cdot\left(\frac{\nu_{\mathrm{T}}}{\sigma_\varepsilon}\nabla\varepsilon\right) + c_{1\varepsilon}\frac{\varepsilon}{k}P_k - c_{2\varepsilon}\frac{\varepsilon^2}{k} \tag{6}$$

where $\sigma_k, \sigma_\varepsilon, c_{1\varepsilon}$ and $c_{2\varepsilon}$ are the empirical turbulence constants and P_k = turbulence production rate defined in a 2D xy plane by

$$P_k = \nu_{\mathrm{T}}\left[2\left(\frac{\partial u}{\partial x}\right)^2 + 2\left(\frac{\partial v}{\partial y}\right)^2 + \left(\frac{\partial u}{\partial y} + \frac{\partial v}{\partial x}\right)^2\right] \tag{7}$$

Although the closure assumptions employed in the k–ε equations are crude, this model has been successfully used to predict many complex flows. The recommended values for the empirical coefficients have been given by Rodi (1993) as $c_{\mathrm{d}} = 0.09$, $\sigma_k = 1.0$, $\sigma_\varepsilon = 1.3$, $c_{1\varepsilon} = 1.44$ and $c_{2\varepsilon} = 1.92$. According to Lin and Liu (1998a), a sensitivity analysis on these parameters showed that a 10% change in $\sigma_k, \sigma_\varepsilon$ and $c_{2\varepsilon}$ only caused less than 10% change in the total turbulence energy, while a 10% change in $c_{1\varepsilon}$ could lead to more than 50% change in the turbulence energy. In spite of some uncertainties involved, the recommended values are adopted for the current SPH computations and the results indicate that they work well.

3 Equation solution processes

The above basic equations are solved through a two-step prediction and correction processes as stipulated by Shao and Lo (2003) and Shao and Gotoh (2005). The first prediction step is an explicit integration in time without enforcing the incompressibility: the gravitational force, the laminar and Reynolds stresses in N–S equation (2) are used and an intermediate particle velocity and position are obtained. At this moment, the incompressibility or mass conservation is not satisfied, which is demonstrated by deviations of the instantaneous particle density from the initial density. Therefore, in the second correction step, the pressure term is used to update particle velocities and positions obtained from the prediction step. The pressure is calculated from a pressure Poisson equation formulated by combining the mass and momentum equations (1) and (2), a semi-implicit approach which is very similar to that employed in a typical grid method (Chorin, 1968). The turbulence properties are updated according to Eqs (5) and (6) after the mean flow field has been solved.

The incompressible SPH model in this paper is different from the original weakly compressible SPH of Monaghan (1992), in that the pressure is determined implicitly from the solution of Poisson equation rather than an equation of state. This algorithm was developed based on the MPS method of Koshizuka *et al.* (1995, 1998), who enforced the incompressibility by keeping the number density of particles being a constant.

4 SPH formulations

In an SPH conception, the motion of each particle is calculated through interactions with neighboring particles using an analytical kernel function. For the fluid flows, all terms in the N–S equations are formulated by particle interaction models and thus a grid is not needed. For a detailed review of the SPH theory see Monaghan (1992). SPH particles move in a Lagrangian coordinates and the advection in N–S equations is directly calculated by particle motion without the numerical diffusion. Each particle can carry a mass m, velocity $\mathbf{u}$ and other properties depending on the problem. For the turbulence modeling, a particle also carries a turbulence eddy viscosity ν_{T}, turbulence energy k and energy dissipation ε. The basic SPH formulations used in the paper are summarized as follows.

The fluid density ρ_a of particle a is evaluated by

$$\rho_a = \sum_b m_b W(|\mathbf{r}_a - \mathbf{r}_b|, h) \tag{8}$$

where a and b = reference particle and its neighbors; m_b = particle mass; $\mathbf{r}_a$ and $\mathbf{r}_b$ = particle positions; W = interpolation kernel and h = smoothing distance, which determines the range of particle interacts and is taken to be 1.2 times of the initial particle spacing in the computations.

The pressure gradient assumes a symmetric form since it conserves the linear and angular momentums

$$\left(\frac{1}{\rho}\nabla P\right)_a = \sum_b m_b\left(\frac{P_a}{\rho_a^2} + \frac{P_b}{\rho_b^2}\right)\nabla_a W_{ab} \tag{9}$$

where the summation is over all particles other than particle a and $\nabla_a W_{ab}$ = gradient of the kernel taken with respect to the positions of particle a.

In a similar way, the velocity divergence of particle a is formulated by

$$\nabla\cdot\mathbf{u}_a = \rho_a\sum_b m_b\left(\frac{\mathbf{u}_a}{\rho_a^2} + \frac{\mathbf{u}_b}{\rho_b^2}\right)\cdot\nabla_a W_{ab} \tag{10}$$

The Reynolds stress in Eq. (2) is formulated by applying the above SPH definition of divergence

$$\left(\frac{1}{\rho}\nabla\cdot\overrightarrow{\tau}\right)_a = \sum_b m_b\left(\frac{\overrightarrow{\tau}_a}{\rho_a^2} + \frac{\overrightarrow{\tau}_b}{\rho_b^2}\right)\cdot\nabla_a W_{ab} \tag{11}$$

The Laplacian for pressure is formulated as a hybrid of a standard SPH first derivative with a finite difference approximation

for the first derivative and represented also in the symmetrical form as

$$\nabla \cdot \left(\frac{1}{\rho}\nabla P\right)_a = \sum_b m_b \frac{8}{(\rho_a + \rho_b)^2} \frac{P_{ab}\mathbf{r}_{ab} \cdot \nabla_a W_{ab}}{|\mathbf{r}_{ab}|^2} \tag{12}$$

where the abbreviations $P_{ab} = P_a - P_b$ and $\mathbf{r}_{ab} = \mathbf{r}_a - \mathbf{r}_b$ are used.

Following this, the laminar viscosity term is formulated by

$$(\nu_0 \nabla^2 \mathbf{u})_a = \sum_b m_b \frac{2(\nu_a + \nu_b)}{\rho_a + \rho_b} \frac{\mathbf{u}_{ab}\mathbf{r}_{ab} \cdot \nabla_a W_{ab}}{|\mathbf{r}_{ab}|^2} \tag{13}$$

where $\mathbf{u}_{ab} = \mathbf{u}_a - \mathbf{u}_b$ is used.

While applying the SPH rules to calculate the element of mean strain rate in Eq. (3), the full derivative between two particles is first obtained using the finite difference and then it is decomposed into x and y directions. Thus

$$\left(\frac{\partial u_i}{\partial x_j}\right)_a = \left(\frac{\partial u_i}{\partial r_{ab}}\right)\left(\frac{\partial x_j}{\partial r_{ab}}\right) = \frac{(u_i)_a - (u_i)_b}{r_{ab}} \frac{(x_j)_a - (x_j)_b}{r_{ab}} \tag{14}$$

where $r_{ab} = |\mathbf{r}_{ab}|$ is the distance between two particles.

5 Treatment of boundary conditions and free surfaces

5.1 Boundary and surface conditions for the SPH particles

The treatment of boundary conditions and free surfaces in the SPH model has already been illustrated in details by Gotoh *et al.* (2004) and Shao and Gotoh (2005). A brief summary is given as follows.

The fixed solid boundaries are treated by fixed wall particles to balance the pressure of inner fluid particles and prevent them from penetrating the wall. The pressure Poisson equation is also solved on these wall particles similar to the treatment of solid walls in a grid method. In order to improve computational accuracy in the near-wall region, a wall function is used to relate velocity at the computational particles closest to bed to the instantaneous shear stress at the bed. A quadratic resistant law based on the logarithmic velocity profile is used. The incident wave is produced by moving a numerical wave paddle located at the offshore boundary, which is treated by moving wall particles. The free surfaces can be easily and accurately tracked by particles in the SPH model, since the particle density on free surface drops significantly due to lack of particles in the outer region of free surface.

5.2 Boundary and surface conditions for the turbulence properties

Appropriate surface and boundary conditions are also needed for the turbulence properties. On the free surface, the zero-gradient boundary conditions are imposed for both the k and ε to ensure the advective and diffusive fluxes of k and ε to be zero, i.e., $\partial k/\partial n = 0$ and $\partial \varepsilon/\partial n = 0$, where n is the unit normal on the free surface. For the SPH particles, this requirement is achieved by setting the values of k and ε of the surface particles equal to those of the particles immediately underneath free surface in the normal direction. Thus there is no turbulence exchange between the air and water.

In theory the turbulence vanishes on the solid walls so that both the k and ε become zero on the wall. However, in practice, the numerical resolution cannot be so fine as to resolve the viscous sub-layer. Thus the boundary conditions for k and ε are generally specified in the turbulent boundary layer instead of right on the wall. Here we follow the approach of Lin and Liu (1998a, b) to use the log law distribution of mean tangential velocities in the turbulent boundary layer, so that the values of k and ε can be expressed as the functions of distance from the solid boundary and the mean tangential velocities outside of the viscous sub-layer.

For the k–ε model, it is also necessary to seed a small amount of k and ε in the initial and inflow boundary conditions. Lin and Liu (1998a, b) and Bradford (2000) used different approaches to seed the initial turbulence properties and unanimously found that the final computational results were insensitive to the initial seeding. In this paper, we reasonably assume that the initial condition should be described in such a way to satisfy $\nu_T \approx \nu_0$, while at the inflow boundary $\nu_T \approx 10\nu_0$ should be applied. It means that the initial turbulence level is quite low in the inner fluid region and slightly higher near the inflow boundary. This leads to the initial seeding values of $k = 2 \times 10^{-5}\,\mathrm{m^2/s^2}$ and $\varepsilon = 4 \times 10^{-5}\,\mathrm{m^2/s^3}$ for the inner fluids and $k = 2 \times 10^{-3}\,\mathrm{m^2/s^2}$ and $\varepsilon = 4 \times 10^{-2}\,\mathrm{m^2/s^3}$ for the inflow boundary. In addition, the initial velocity of fluid particles is set zero and the initial pressure is assumed to be hydrostatic.

6 Numerical simulations of wave breaking on a slope—spilling and plunging breakers

6.1 Experimental setup

The detailed experimental setup has been given in the initial paper of Ting and Kirby (1994). Here only some important parameters are summarized. A beach with constant slope of $s = 1/35$ is connected to a region with constant water depth of $d_c = 0.4\,\mathrm{m}$. The coordinate system is chosen so that the origin $x = 0.0\,\mathrm{m}$ is located at the position where the still water depth is $d_0 = 0.38\,\mathrm{m}$ and $y = 0.0\,\mathrm{m}$ is located at the still water surface. According to Ting and Kirby (1994), a sketch view of the experimental setup is shown in Fig. 1. The following notations are used in the

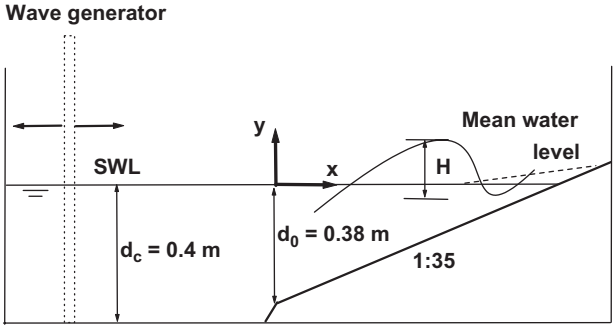

Figure 1 Sketch view of experimental setup (Ting and Kirby, 1994).

study: ζ_{mean} denotes the mean water level measured with respect to the still water level, ζ_{crest} is the crest height and ζ_{trough} represents the trough level. h is the mean water depth, h_b is the water depth at breaking point and $c = \sqrt{gh}$ is the wave celerity estimated by the shallow water linear theory. The wave height H is defined as the distance between the wave crest and trough.

In the experiment, the incident cnoidal wave had a height $H = 0.125$ m and period $T = 2.0$ s for the spilling breaker case, while $H = 0.128$ m and $T = 5.0$ s were used to generate a plunging breaker. The laboratory experiment recorded a breaking wave height $H_b = 0.1625$ m at $x_b = 6.4$ m for the spilling breaker and $H_b = 0.190$ m at $x_b = 7.795$ m for the plunging breaker, respectively.

6.2 Computational parameters

The incompressible SPH method coupled with a k–ε turbulence model is employed to reproduce the above experiment. The computational domain is taken to be 20.0 m long, covering from $x = -4.0$ m to $x = 16.0$ m. The time step Δt is automatically adjusted in the computation, satisfying the stability requirements of Courant condition and viscous diffusion. By considering the computational efficiency, the initial particle spacing is chosen as $\Delta X = 0.02$ m and approximately 12,000 particles are employed in the computation. The fluid particles are initially arranged on a regular, equally spaced grid system, with boundary particles added to form the horizontal bed, slope and offshore wavemaker.

In the following analyses, the numerical results of both spilling and plunging breakers are extracted from $t = 12T$, from which the computed velocities and free surface profiles indicate that the computed waves in the surf zone have almost reached the steady state and the set-up and set-down have fully developed. The time scale is longer than $t = 8T$ adopted by Lin and Liu (1998a) and $t = 10T$ adopted by Bradford (2000) in the simulations of a similar case.

6.3 Wave transformation and breaking characteristics

The instantaneous SPH particle snapshots of the 12th breaking wave are shown in Figs 2(a–c) and 3(a–c), respectively, for the spilling and plunging breakers. It is seen that the general features of wave breaking, collapsing and subsequent turbulent bore formation have been well captured by the SPH computations. The simulated wave breaking processes are very similar to those found by Lin and Liu (1998a, b) and Bradford (2000) in the numerical computations and Ting and Kirby (1994, 1995, 1996) in the experiments. The spilling breaker is a milder wave breaking process, in which the wave keeps its quasi-symmetric form up to the final collapse and the wave height decreases gradually as shown in Fig. 2(a–c). In comparison, the plunging breaker is much more violent and the wave shape deforms drastically after the breaking as shown in Fig. 3(a–c). The overturning of the wave front at breaking is qualitatively captured by the SPH computations in Fig. 3(b). The curling forward of wave crest hits the surface of wave trough and the impact of the jet pushes up a wedge of water to form a new wave at $t = 0.2T$ as seen in

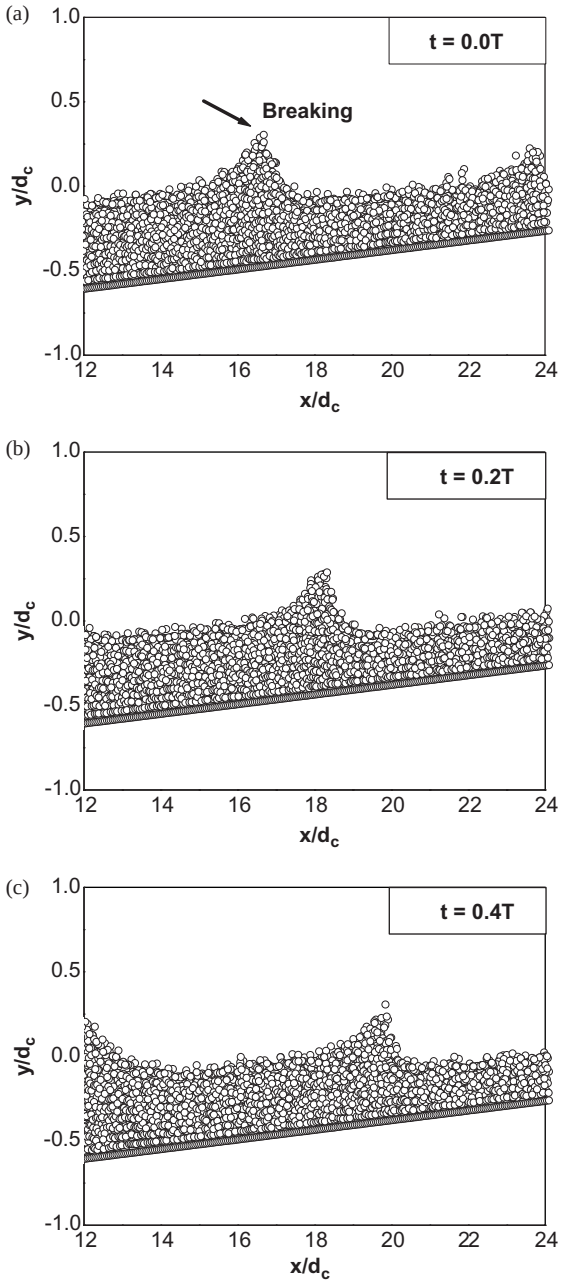

Figure 2(a–c) Instantaneous particle snapshots of spilling wave.

Fig. 3(c). Bradford (2000) did not find the overturning of the wave front even a much finer grid was used. Lin and Liu (1998b) did find this phenomenon by performing a higher resolution simulation of plunging wave, but the computation was carried out in a constant water depth. In contrast, the SPH computations adequately reproduce the curling forward of the plunging front using a relatively coarser particle spacing of $\Delta X = 0.02$ m. This is due to that the SPH approach has the advantage of treating free surfaces of large deformation without the numerical diffusion, which is inevitable in an Eulerian grid method. In spite of the fact that the VOF method used by Lin and Liu (1998b) and Bradford (2000) theoretically possesses the ability to model complex free surface geometries and fluid detachment, a strict spatial resolution is required.

Further examining the instantaneous velocity fields of spilling and plunging waves in Figs 4(a–c) and 5(a–c) shows that the

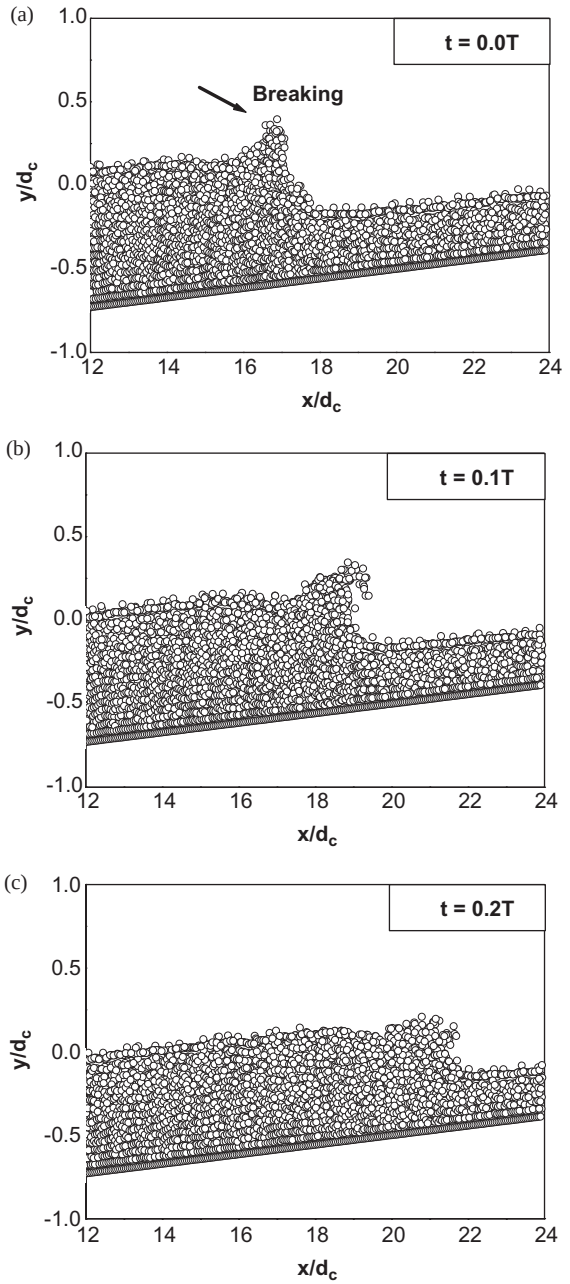

Figure 3(a–c) Instantaneous particle snapshots of plunging wave.

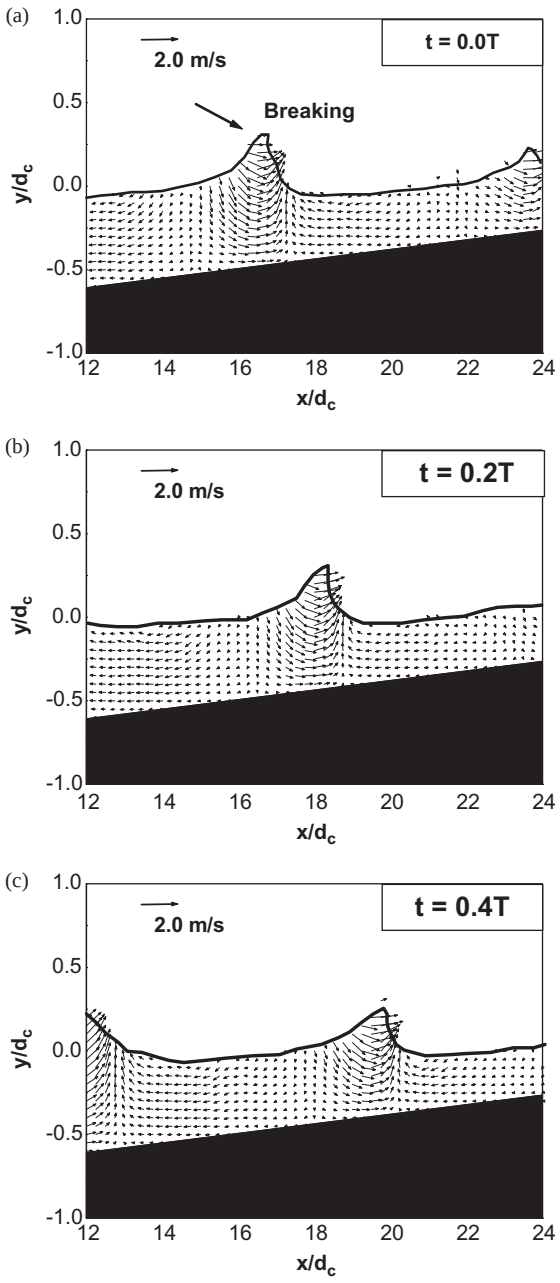

Figure 4(a–c) Instantaneous velocity fields of spilling wave.

velocities under the spilling breaker are quite similar to those under a non-breaking wave found from the liner wave theory, except that slightly larger velocities appear at the wave front. On the other hand, the velocity distributions of the plunging breaker deviate significantly from the linear wave theory and the magnitude of the velocity is also much higher. At $t = 0.1T$ after the breaking as shown in Fig. 5(b), a plunging jet with maximum velocity of 3.5 m/s impacts toward the wave trough and generates a turbulent bore with a velocity of 2.5 m/s at $t = 0.2T$, as shown in Fig. 5(c). The velocity field immediately underneath the wave trough of the impingement is greatly modified by the penetration of the plunging jet. In contrast, the maximum velocity of the spilling breaker in Fig. 4 is found to be only 1.5 m/s.

The above general wave transformation and breaking processes indicate that the plunging breaker has a very obvious transitional stage, during which the wave rapidly changes the shape and dissipates the energy. The spilling breaker, however, produces the final quasi-steady turbulent bore with negligible notice. From this point, we could reasonably propose that the depth-averaged equations such as the shallow-water equation should perform well in the simulations of a spilling breaker, provided that the turbulence dissipation mechanism is given suitable consideration. But as for the plunging model, lots of work should be done to test the accuracy of the depth-averaged equations in the transitional stage (Lin and Liu, 1998b).

6.4 Comparisons and analyses of wave surface profiles

The computed distributions of the mean water levels, the wave crest and trough elevations by the SPH model are shown in Figs 6 and 7, respectively, for the spilling and plunging waves.

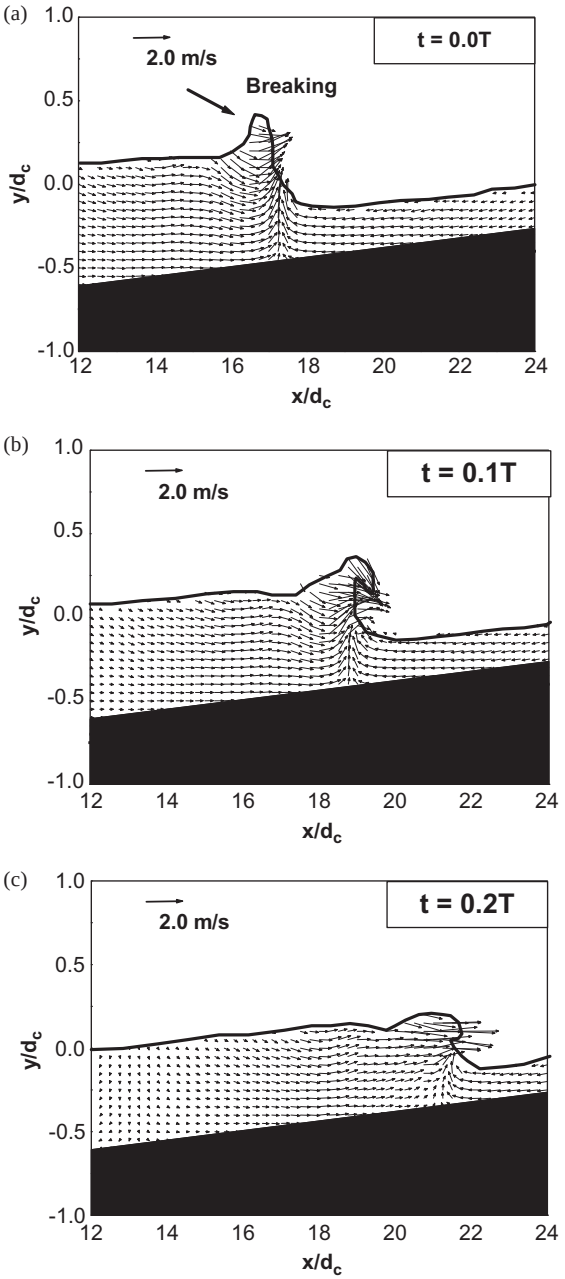

Figure 5(a–c) Instantaneous velocity fields of plunging wave.

Meanwhile, the experimental data of Ting and Kirby (1994) and numerical results of Bradford (2000) are shown for comparison. It should be mentioned that Bradford (2000) used different turbulence models in the computations and found that the k–ε model gave the best match to the surface elevations and the RNG model gave the best match to the undertow and turbulence profiles. Here we use the best results of Bradford (2000) to validate the SPH computations.

Figure 6 shows the comparisons for the spilling breaker. It is seen that the model predictions by both the SPH and Bradford (2000) closely match the trough and mean water levels. However, the wave crest is underpredicted before and after the breaking by Bradford (2000). The SPH computations underpredict the crest level before the breaking but overpredict it after the breaking. The breaking point is defined at which the maximum wave height is obtained. The experiment (Ting and Kirby, 1994) recorded a breaking wave height $H_b/d_c = 0.406$ at $x_b/d_c = 16.0$

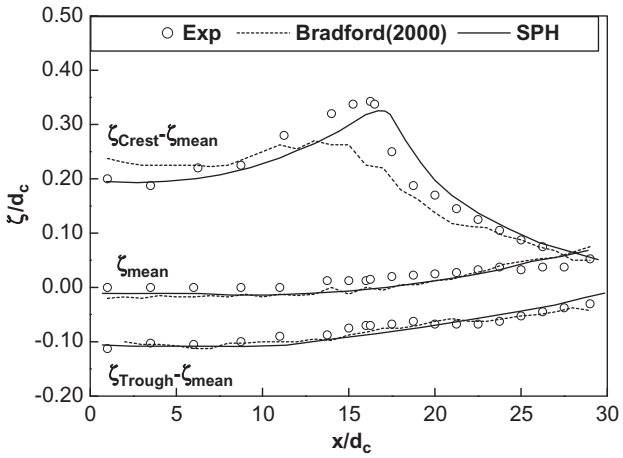

Figure 6 Computational and experimental mean water levels, wave crest and trough elevations of spilling wave.

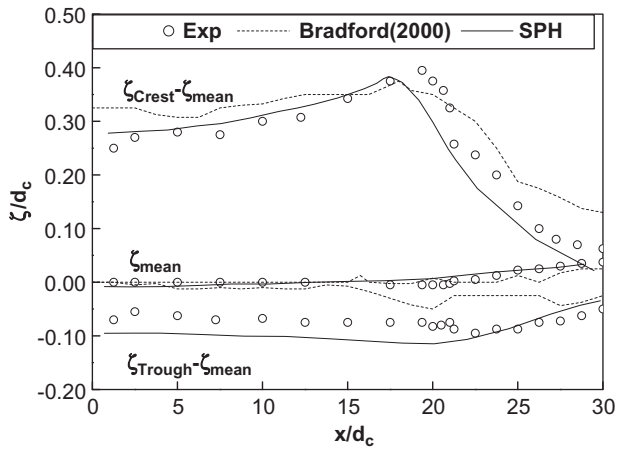

Figure 7 Computational and experimental mean water levels, wave crest and trough elevations of plunging wave.

for the spilling breaker. The k–ε model of Bradford (2000) predicted a breaking wave height $H_b/d_c = 0.348$ at $x_b/d_c = 12.78$, which is earlier than the real breaking. In comparison, the SPH computations predict a breaking wave height $H_b/d_c = 0.385$ at $x_b/d_c = 17.0$, which is later than the real breaking. Bradford (2000) performed a sensitivity analysis by refining the grid size and deactivating the turbulence, but there was no much improvement in the predictions of the breaking height and locations. He attributed the discrepancies to the inadequate descriptions of wave dynamics at the inflow boundary. A similar work is also done using the SPH runs and it is found that the breaking position is really quite sensitive to the inflow condition. However, both the k–ε trials of Bradford (2000) and SPH computations agree in that the predicted breaking wave height H_b is insensitive to the particular choice of the inflow wave theory.

For the plunging wave as shown in Fig. 7, the predictions by SPH model are also generally better than those obtained by Bradford (2000). The experiment of Ting and Kirby (1994) in this case yielded a breaking wave height $H_b/d_c = 0.475$ at $x_b/d_c = 19.49$. The k–ε model of Bradford (2000) reported a breaking wave height $H_b/d_c = 0.405$ at $x_b/d_c = 18.13$ and the SPH model reports a breaking wave height $H_b/d_c = 0.495$ at

$x_b/d_c = 17.4$. This indicates that a larger wave height can be obtained by the SPH approach, since it uses particles to track the free surfaces without numerical diffusion. It is quite obvious that both numerical models poorly predict the trough level. Bradford (2000) continuously overpredicted the wave trough, while the SPH computations underestimate the trough prior to the breaking but slightly overestimate it after the breaking. Here we attribute the failure of accurately reproducing the wave trough to the insufficient length of the computational domain. The generated plunging wave has a period of $T = 5$ s. By using the cnoidal wave theory, the corresponding wave length is estimated to be 10.8 m in a constant water depth of $d_c = 0.4$ m. The horizontal section of the computational domain for the SPH runs and probably adopted by Bradford (2000) cannot meet this requirement. As a result, the wave has already started shoaling over the slope prior to the full development in the constant depth, which could cause the large discrepancy between the computational and experimental wave trough levels.

6.5 *Comparisons and analyses of undertow and turbulence quantities*

In order to further verify the accuracy of the SPH model, the computed mean undertow velocities and turbulence intensities are compared with the experimental data of Ting and Kirby (1994) and numerical results of Bradford (2000) in Figs 8(a, b) and 9(a, b), for the spilling and plunging breakers, respectively. In the spilling breaker case, the comparisons are made at locations of $(x - x_b)/h_b = 4.397$ and 10.528. As for the plunging breaker, the comparisons are made at $(x - x_b)/h_b = 3.571$ and 12.987. The mean quantities are obtained by averaging over the successive numerical wave data from $t = 12T$ to $t = 20T$. In all the figures, the vertical length scale is normalized by the local water depth h and the undertow velocities and turbulence intensities are normalized by the wave celerity $c = \sqrt{gh}$.

It is shown from Figs 8 and 9 that both the magnitude and the vertical distributions of the mean quantities are reasonably predicted in all cases. However, the computations by two numerical models match the experiment better for the plunging wave as compared with the spilling wave. It is also found that under the plunging breaker, the vertical variations of undertow and turbulence quantities are smaller than those under the spilling breaker. This is due to that the vertical mixing is much larger in the plunging wave, which reduces the vertical gradients and thus makes the problem easier to solve.

It should be noticed here that the SPH computations generally overestimate the turbulence levels. The overpredictions are much more obvious for the spilling wave than for the plunging wave. For example, the turbulence intensities are overestimated by a maximum value of 64% for the spilling wave in Fig. 8(a) and a maximum value of 52% for the plunging wave in Fig. 9(a). Besides, the overpredictions are much more predominant in the inner surf zones rather than the outer surf zones, according to the classifications by Ting and Kirby (1994, 1995, 1996). The same problem was also reported by Lin and Liu (1998a, b). They concluded that the source of discrepancy could be traced to the use of constant coefficients in the k–ε model. These coefficients have been derived from the quasi-steady flows and thus may behave

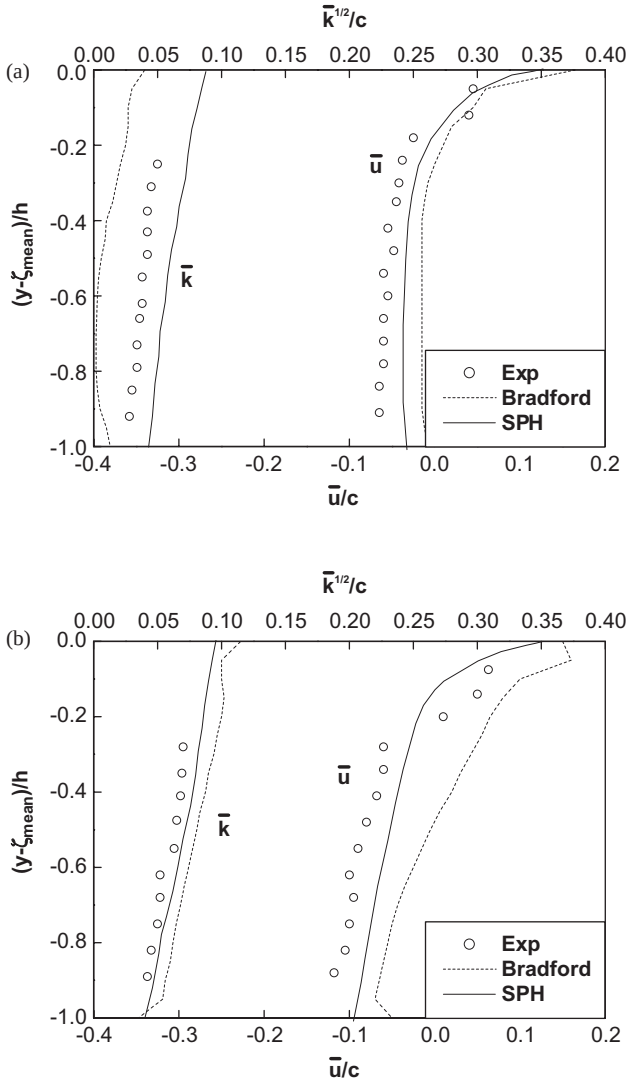

Figure 8 Computational and experimental mean undertow velocities and turbulence intensities at locations of (a) $(x - x_b)/h_b = 4.397$ and (b) $(x - x_b)/h_b = 10.528$ for spilling wave.

poorly in a strongly transient turbulence flow such as the initial breaking wave. In addition, they further concluded that this problem only localized near the breaking wave front, and in the surf zones away from the breaking front the turbulence intensities could be well predicted by the k–ε model using the recommended coefficients.

The accurate prediction of the undertows is of great importance to the prediction of the sediment motion, since the vertical gradient of the suspended sediment concentration is very sensitive to the shape of undertow profiles. However, much finer resolutions and longer computations are needed to accurately capture the existence of the undertow currents. Figures 8 and 9 indicate that although obvious discrepancies with the experiment exist, the SPH computations predict a relatively stronger undertow as compared with a weaker one predicted by Bradford (2000) using the RNG model. The primary reason for the difference is attributed to the insufficient computational time in the simulations of Bradford (2000), in which the waves might not have attained the quasi-steady state and the full set-up and set-down might

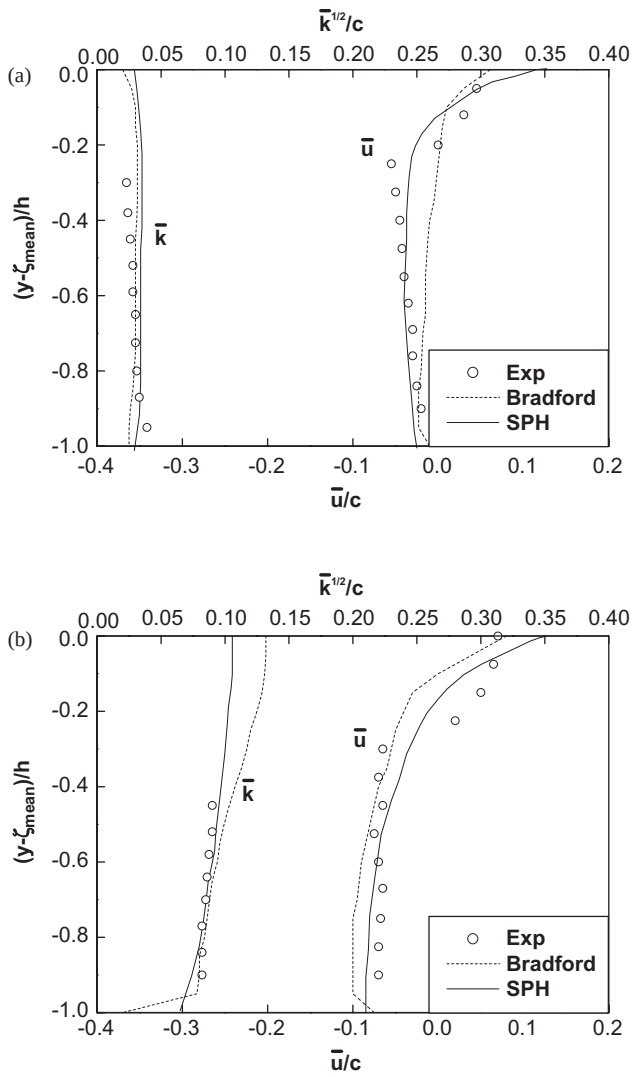

Figure 9 Computational and experimental mean undertow velocities and turbulence intensities at locations of (a) $(x - x_b)/h_b = 3.571$ and (b) $(x - x_b)/h_b = 12.987$ for plunging wave.

not have fully developed. In the SPH runs, the mean values are obtained by averaging the numerical wave data from $t = 12T$ to $t = 20T$. In comparison, Bradford (2000) averaged the wave data over $5T$ up to $t = 10T$ for the spilling wave and over $3T$ up to $t = 6T$ for the plunging wave. Recently, a perfect agreement between the computational and experimental undertow profiles was reported by Lin and Liu (2004) for an identical spilling wave, in which the mean average was computed from $t = 25T$ to $t = 30T$.

6.6 Spatial and temporal evolutions of turbulence quantities

One of the great advantages of the numerical models is their ability to disclose the evolutions of turbulence quantities in the spatial and temporal domains. Using the SPH computational results, the turbulence intensity distributions are shown in Figs 10(a–c) and 11(a–c), respectively, for the spilling and plunging waves. Inside the figures, the turbulence quantities are normalized by the wave celerity $c = \sqrt{gh}$ and only high turbulence areas are displayed for clarity.

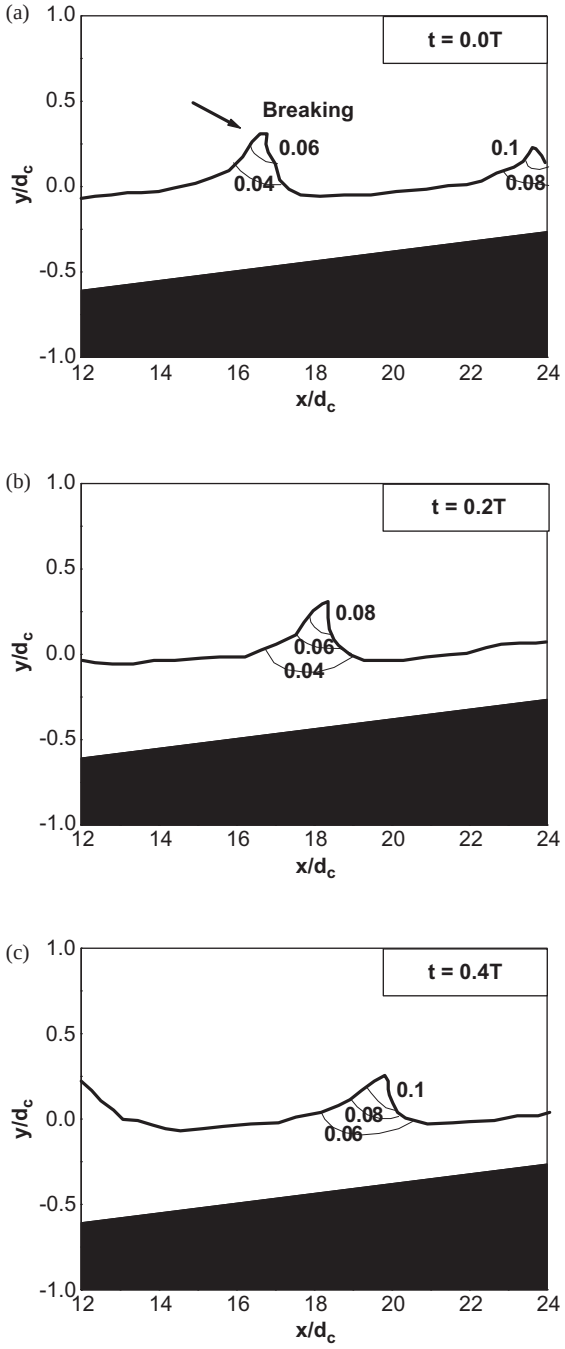

Figure 10(a–c) Turbulence intensity distributions $k^{1/2}/c$ of spilling wave.

It is shown that there exist fundamental differences in the dynamics of turbulence between the spilling and plunging breakers, which can be related to the processes of wave breaking and turbulence production. For the spilling wave as shown in Fig. 10, the high turbulence area is mainly concentrated in the breaking wave front. In other regions, the turbulence quantity is rather small, which suggests that the mean flow has little influence from the breaking process. The highest turbulence level $k^{1/2}/c = 0.08$–0.1 appears in the roller region. As the wave propagates forward, the turbulence kinetic energy gradually changes but with very similar patterns of the turbulence distributions accompanied by the decaying wave amplitude.

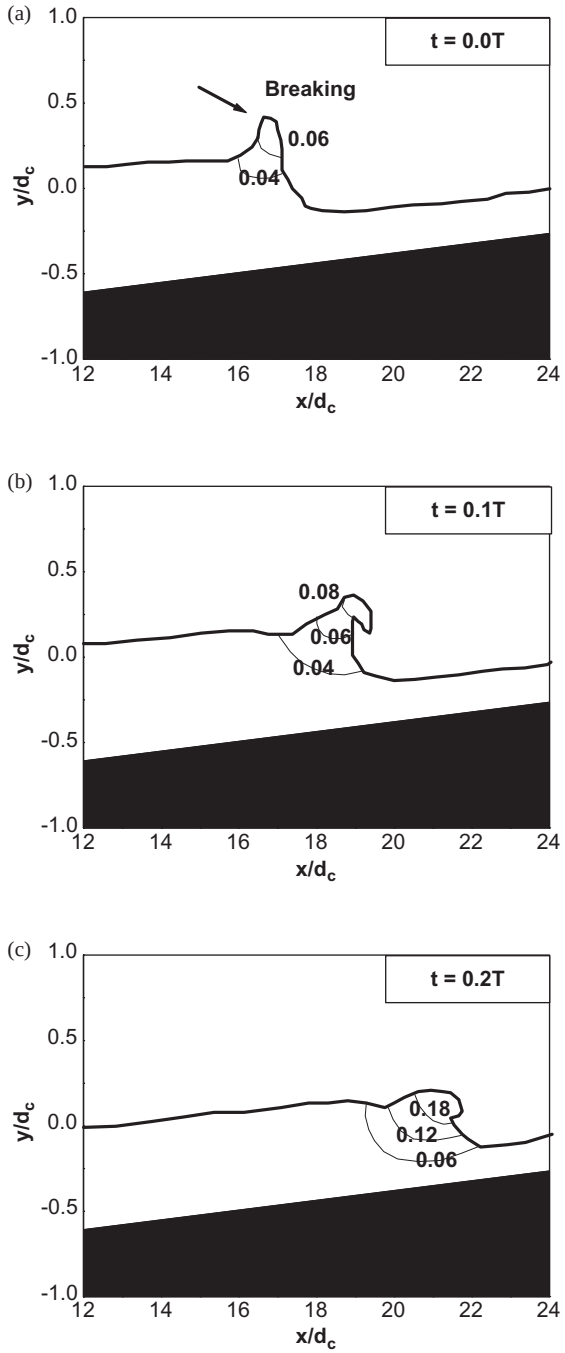

Figure 11(a–c) Turbulence intensity distributions $k^{1/2}/c$ of plunging wave.

On the other hand, the turbulence levels increase rapidly after the wave breaking for the plunging case as shown in Fig. 11. The maximum turbulence level $k^{1/2}/c = 0.12 - 0.18$ is generated almost instantly as the plunging jet touches down on the wave trough. The roller continues to spread downwards as the breaking wave front propagates downstream and penetrates as deep as half the water depth, which is shown at $t = 0.2T$ in Fig. 11(c). In comparison, the roller is essentially confined to the top of the wave front for the spilling breaker in Fig. 10. As a result, on the middle elevation, the turbulence transport is much stronger for the plunging wave than for the spilling wave. However, our computations further indicate that the initial geometry and strength of the plunging jet generally only have local influence to the wave motion and have little impact on the turbulence transport mechanisms a short distance away from the plunging point.

The above turbulence production and development processes are well consistent with the experimental observations of Ting and Kirby (1994, 1995, 1996) and the numerical simulations of Lin and Liu (1998a, b) and Bradford (2000). From this point, it can be reasonably concluded that the different kinds of wave breakers can be distinguished not only by the surface profiles but also by the turbulence fields under the breaking front. Based on the analyses of the turbulence characteristics, we further propose that the potential flow theory could be applied to the non-breaking and pre-breaking waves with enough accuracy, but great attentions should be paid to the region near the wave breaking front and more advanced modeling technique is needed to address this local issue.

6.7 Limitations of numerical approach

Although good agreement with the literature is achieved in the SPH computations, there exist some uncertainties about the simulation results and the numerical approach is limited by several factors. For example, the wave breaking is a two-phase problem. Especially in the plunging waves, the entrapped air leads to the increased air entrainment and formation of bubbles in the water, which strongly influences the subsequent breaking waves. Unfortunately, this issue is not addressed by the present SPH model. Besides, the undertow velocities are still underpredicted due to the inadequate run time. In the SPH computations, the time-mean average is calculated using successive wave data over $8T$ from $t = 12T$ to $t = 20T$, while 102 successive wave data were used in the experiment of Ting and Kirby (1994). As previously mentioned, it is remarkably noticed that the turbulence level is overpredicted in all the cases. The primary reason is due to that the coefficients used in the k–ε model were obtained from the experiments for steady flows rather than oscillatory flows. There are still strong needs to further improve the performance of turbulence closure models. The intrusions of air in the roller and upper area of the surf zone might also account for the deviations between the numerical and experimental turbulences.

The repeatability of the computations provides a useful check for numerical models dealing with the periodical flow simulations. Since the wave breaking events in this study have a repeatable occurrence, highly reproducible computational waves are also essential to ensure the accurate predictions of the undertow and turbulence quantities. To investigate the repeatability of SPH computations, we made simple analyses on time series of the calculated breaking wave height H_b, for each of the waves between $t = 12T$ and $20T$. The results indicate that there is a variation of 5% in H_b for the spilling breaker and the variation is 8% for the plunging breaker. This suggests that the differences between each flow due to the phase differences are small and the periodical motions of the breaking waves are well reproduced. However, the exact repeatability cannot be maintained in practice, because the wave breaking is a non-deterministic process and the turbulence has a random nature and affects the repeatable flows. The analyses also show that the variations in the breaking wave

height are larger in the plunging wave rather than in the spilling wave, which is consistent with the previous conclusion that the turbulence levels in the former are higher than those in the latter.

7 Conclusions

The paper presents an incompressible SPH method coupled with k–ε model to simulate the spilling and plunging waves. The numerical results are in good agreement with the documented data. The particle approach gives the better predictions of the wave surface profiles, turbulence and undertow quantities as compared with the predictions by the Euler grid method in the tested range. The SPH model is shown to be capable of accurately tracking the free surfaces without the numerical diffusion. The k–ε model is found to be a simple and effective tool to deal with the turbulence under the breaking waves even if constant coefficients are used for the model. It is disclosed that under the plunging breaker, the wave deformations and turbulence levels are much larger and the vertical variations of the undertow and turbulence quantities are much smaller, as compared with the spilling breaker. The study indicates that there are fundamental differences in the wave dynamics between the spilling and plunging waves, which are disclosed by the wave breaking processes and the turbulence evolutions.

Additional work is needed to address the influence of air bubbles in the breaking waves. A two-phase SPH model incorporating the water–air interactions will be developed in the future work.

Acknowledgments

The numerical SPH code in the paper has been developed and improved based on the moving particle semi-implicit (MPS) code provided by Professor Seiichi Koshizuka, Department of Quantum Engineering and Systems Science, Graduate School of Engineering at The University of Tokyo. His guidance on the SPH coding process is greatly appreciated. The author is equally grateful to his previous supervisors Professor Edmond Yat Man Lo, School of Civil and Environmental Engineering at Nanyang Technological University and Professor Hitoshi Gotoh, Department of Urban and Environmental Engineering at Kyoto University, for their guidance on the SPH and turbulence modeling when the author was working in Singapore and Japan. Besides, the invaluable comments and suggestions of Professor Niansheng Cheng at Nanyang Technological University significantly improved the quality of the paper. The author also acknowledges the support of Japan Society for the Promotion of Science (JSPS) and University of Plymouth provided through a postdoctoral research fellowship.

Notation

c = Wave celerity
$c_{1\varepsilon}$ = Turbulence constant
$c_{2\varepsilon}$ = Turbulence constant
c_d = Turbulence constant
d_0 = Still water depth at origin
d_c = Constant water depth
$\mathbf{g}$ = Gravitational acceleration
h = Kernel smoothing distance or mean water depth
h_b = Water depth at breaking point
H = Wave height defined as distance between wave crest and trough
H_b = Wave height at breaking point
k = Turbulence kinetic energy
$\bar{k}$ = Time-mean turbulence kinetic energy
m = Particle mass
n = Unit normal on free surface
P = Pressure
P_k = Turbulence production rate
r = Distance between particles
$\mathbf{r}$ = Position vector
s = Slope of beach
S_{ij} = Element of strain rate
T = Wave period
$\mathbf{u}$ = Velocity vector
$\bar{u}$ = Time-mean undertow velocity
W = Interpolation kernel
x_b = Horizontal coordinate at breaking point
δ_{ij} = Kronecker delta
Δt = Time increment
ΔX = Particle spacing
ε = Turbulence dissipation rate
ζ_crest = Wave crest level
ζ_mean = Mean water level
ζ_trough = Wave trough level
ν_0 = Kinetic viscosity of laminar flow
ν_T = Turbulence eddy viscosity
ρ = Fluid density
σ_k, σ_ε = Turbulence constants
$\vec{\tau}$ = Reynolds stress
τ_{ij} = Element of Reynolds stress

Subscripts and symbols

a = Reference particle
ab = Values between particle a and b
b = Neighboring particle
t = Time
x = Horizontal coordinate
y = Vertical coordinate

References

1. BRADFORD, S.F. (2000). "Numerical Simulation of Surf Zone Dynamics". *J. Wtrwy. Port Coast. Oceanic Engng. ASCE* 126(1), 1–13.
2. CHORIN, A.J. (1968). "Numerical Solution of the Navier–Stokes Equations". *Math. Comp.* 22, 745–762.

3. GOTOH, H., SHAO, S.D. and MEMITA, T. (2004). "SPH-LES Model for Numerical Investigation of Wave Interaction with Partially Immersed Breakwater". *Coast. Engng. J.* 46(1), 39–63.
4. HARLOW, F.H. and WELCH, J.E. (1965). "Numerical Calculation of Time-Dependent Viscous Incompressible Flow of Fluid with Free Surface". *Phys. Fluids* 8(12), 322–329.
5. HIRT, C.W. and NICHOLS, B.D. (1981). "Volume of Fluid (VOF) Method for the Dynamics of Free Boundaries". *J. Comput. Phys.* 39, 201–225.
6. KOSHIZUKA, S., TAMAKO, H. and OKA, Y. (1995). "A Particle Method for Incompressible Viscous Flow with Fluid Fragmentation". *Comput. Fluid Dyn. J.* 4, 29–46.
7. KOSHIZUKA, S., NOBE, A. and OKA, Y. (1998). "Numerical Analysis of Breaking Waves Using the Moving Particle Semi-Implicit Method". *Int. J. Numer. Meth. Fluids* 26, 751–769.
8. LIN, P.Z. and LIU, L.F. (1998a). "A Numerical Study of Breaking Waves in the Surf Zone". *J. Fluid Mech.* 359, 239–264.
9. LIN, P.Z. and LIU, L.F. (1998b). "Turbulence Transport, Vorticity Dynamics, and Solute Mixing Under Plunging Breaking Waves in Surf Zone". *J. Geophys. Res.* 103(C8), 15677–15694.
10. LIN, P.Z. and LIU, L.F. (2004). "Discussion of Vertical Variation of the Flow Across the Surf Zone". *Coast. Engng.* 50, 161–164.
11. LONGO, S., PETTI, M. and LOSADA, I.J. (2002). "Turbulence in the Swash and Surf Zones: A Review". *Coast. Engng.* 45, 129–147.
12. MONAGHAN, J.J. (1992). "Smoothed Particle Hydrodynamics". *Annu. Rev. Astron. Astrophys.* 30, 543–574.
13. MONAGHAN, J.J. (2002). "SPH Compressible Turbulence". *Mon. Not. R. Astron. Soc.* 335, 843–852.
14. RODI, W. (1993). *Turbulence Models and Their Application in Hydraulics—A State-of-the-Art Review*. IAHR Monograph, Balkema, The Netherlands.
15. ROGALLO, R.S. and MOIN, P. (1984). "Numerical Simulation of Turbulent Flows". *Annu. Rev. Fluid Mech.* 16, 99–137.
16. SHAO, S.D. and LO, Y.M. (2003). "Incompressible SPH Method for Simulating Newtonian and Non-Newtonian Flows with a Free Surface". *Adv. Water Resour.* 26(7), 787–800.
17. SHAO, S.D. and GOTOH, H. (2005). "Turbulence Particle Models for Tracking Free Surfaces". *J. Hydraul. Res.* 43(3), 276–289.
18. TING, F.C.K. and KIRBY, J.T. (1994). "Observation of Undertow and Turbulence in a Laboratory Surf Zone". *Coast. Engng.* 24, 51–80.
19. TING, F.C.K. and KIRBY, J.T. (1995). "Dynamics of Surf-Zone Turbulence in a Strong Plunging Breaker". *Coast. Engng.* 24, 177–204.
20. TING, F.C.K. and KIRBY, J.T. (1996). "Dynamics of Surf-Zone Turbulence in a Spilling Breaker". *Coast. Engng.* 27, 131–160.
21. VIOLEAU, D., PICCON, S. and CHABARD, J.P. (2001). "Two Attempts of Turbulence Modeling in Smoothed Particle Hydrodynamics". *Proceedings of the Eighth International Symposium on Flow Modeling and Turbulence Measurements*, Tokyo, Japan, 4–6 December.